NANO LETTERS

2008
Vol. 8, No. 9
2800-2805

Noninvasive Raman Spectroscopy in Living Mice for Evaluation of Tumor Targeting with Carbon Nanotubes

C. Zavaleta,[†] A. de la Zerda,[†] Z. Liu,[‡] S. Keren,[†] Z. Cheng,[†] M. Schipper,[†] X. Chen,[†] H. Dai,[‡] and S. S. Gambhir*[,†]

Molecular Imaging Program at Stanford, Departments of Radiology and Bioengineering, Bio-X Program, Stanford University, 1201 Welch Road, Stanford, California 94305-5484, and Department of Chemistry, Stanford University, Stanford, California 94305

Received May 12, 2008; Revised Manuscript Received June 27, 2008

ABSTRACT

An optimized noninvasive Raman microscope was used to evaluate tumor targeting and localization of single walled carbon nanotubes (SWNTs) in mice. Raman images were acquired in two groups of tumor-bearing mice. The control group received plain-SWNTs, whereas the experimental group received tumor targeting RGD-SWNTs intravenously. Raman imaging commenced over the next 72 h and revealed increased accumulation of RGD-SWNTs in tumor ($p < 0.05$) as opposed to plain-SWNTs. These results support the development of a new preclinical Raman imager.

Raman spectroscopy is a well established bioanalytical tool with many advantages including excellent sensitivity to small structural and chemical changes, minimal sample preparation, high spatial resolution, and resistance to autofluorescence and photobleaching.[1] Although scientists have reported the use of Raman spectroscopy to image biological processes within living cells and excised tissues, [2−7] its inherently weak effect has limited its application to noninvasively assess small animal models. However, with careful system design and appropriate modifications, our laboratory has developed a Raman microscope capable of noninvasive deep tissue imaging.[8]

The current paper focuses on the ability of our optimized Raman microscope to effectively localize functionalized single wall nanotubes (SWNTs) in a tumor model. Carbon nanotubes have played a fundamental role in the rapidly developing field of nanotechnology because of their unique properties and high potential in biomedical applications including targeted chemotherapeutics, diagnostic imaging contrast agents, and photoablative therapy agents.[9,10] Absence of acute toxicity, relatively long circulation time, and rapid renal clearance also make SWNTs an attractive diagnostic and therapeutic nanodevice.[9,11] Raman spectroscopy has proven to be a valuable tool for characterizing SWNTs. The inherent Raman peak, referred to as the G-band (∼1593 cm^{-1}), is associated with the graphite in SWNTs and makes them ideal for high sensitivity detection with our Raman microspectroscopy system.[8]

These quasi-one-dimensional structures (Supporting Information (SI) Figure 1) are also ideal for modification with biomolecules because of their carbon nanostructure and have been recently used in tumor targeting.[7] Liu et al. investigated the biodistribution of radio-labeled SWNTs in mice by positron emission tomography (PET), ex-vivo biodistribution and invasive Raman spectroscopy of excised tissues. They concluded efficient targeting in mice of $\alpha_v\beta_3$ integrin positive tumor (U87MG tumor model) with pegylated SWNTs linked to an arginine-glycine-asparatic acid (RGD) peptide.[7] Integrin $\alpha_v\beta_3$ is highly expressed on endothelial cells undergoing angiogenesis and solid tumor cells, thus becoming a promising diagnostic and therapeutic target for various solid tumors.[12] RGD peptides that are integrin specific can be used for the development of new noninvasive methods to localize and quantify integrin $\alpha_v\beta_3$ expression in cancer patients.[13,14] This could potentially lead to better diagnosis in selecting patients for anti-integrin treatment and post therapeutic monitoring for treatment efficacy. MicroPET has been recently investigated as a useful diagnostic tool in imaging tumor integrin $\alpha_v\beta_3$ expression in small animal models with copper-64 (^{64}Cu) and fluorine-18 (^{18}F) labeled RGD peptides.[7,15,16]

Using microPET to evaluate effective targeting, involves the use of additional labeling of radioactive material to SWNTs. Additionally, in the RGD conjugated SWNT study

* To whom correspondence should be addressed: Phone: 650-725-2309. Fax: 650-724-4948. E-mail: sgambhir@stanford.edu.
[†] Departments of Radiology and Bioengineering, Bio-X Program, Stanford University.
[‡] Department of Chemistry, Stanford University.

10.1021/nl801362a CCC: $40.75
Published on Web 08/07/2008

reported by Liu et al., animals were sacrificed at 8 hours for tissue evaluation with Raman imaging preventing longitudinal assessment of tumor targeting. Our optimized system takes advantage of the inherent Raman peak of the graphite structure in SWNTs to noninvasively image internal tissue systems (i.e., liver, tumor models) over an extended period of time in the same mouse without adding radioactive isotopes that could potentially influence experimental therapeutic outcome. In addition, the modification of SWNTs with both a DOTA (1,4,7,10-tetraazacyclododecane-1,4,7,10-tetraacetic acid) metal chelator and an RGD peptide is difficult to prepare; and the radiolabeling procedure can be costly and time-consuming involving unnecessary radiation exposure. We investigated the potential of our Raman system to noninvasively localize targeting of RGD nanotubes in a U87MG tumor model in mice over several days. The noninvasive Raman imaging results were compared with excised tissues and are consistent with the Liu paper (which used radiolabeling and invasive Raman analysis of excised tissue samples) showing effective targeting of RGD-SWNTs to the tumor area as opposed to plain SWNTs.

As a first step, we characterized the sensitivity of our Raman microscope in conjunction with SWNTs by subcutaneously injecting mice with decreasing concentrations of SWNTs nanoparticles in a volume of 20 μL (10 μL of SWNTs and 10 μL of matrigel). The data revealed a highly linear relationship between calculated and injected concentration of nanoparticles with an $R^2 = 0.97$. The smallest amount of SWNTs detected in a 20 μL subcutaneous injection was 0.6 nM.

Next, an in vitro cell study was performed to evaluate the targeting potential of our RGD conjugated SWNTs to an $\alpha_v\beta_3$ integrin positive tumor cell line (U87MG). Raman analysis revealed a 75% increase in signal in U87MG cells that were incubated with RGD-SWNTs as opposed to U87MG cells incubated with plain SWNTs ($p < 0.05$). In addition, a negative $\alpha_v\beta_3$ integrin cell line (HT29) was incubated with RGD-SWNTs to reveal a 195% decreased signal than the U87MG cell line incubated with RGD-SWNTs ($p < 0.05$). Cells incubated with phosphate buffered saline (PBS) showed negligible Raman signal when compared to any of the groups ($p < 0.05$)

The maximum depth of penetration for our Raman microscope was also evaluated using a tissue mimicking phantom where a maximum depth of 2 mm was observed under the exact conditions used in this experiment (SNWT concentration and uptake in tumor was based on previous work done by Liu et al.).[7]

After the completion of these initial characterization experiments, we began the noninvasive in vivo evaluation of our Raman microscope's ability to monitor tumor targeting with functionalized SWNTs. Pharmacokinetics of SWNT accumulation in the tumor was evaluated with dynamic Raman imaging at various time points over 30 min immediately following an intravenous injection of 60 pmol of SWNTs in the experimental (RGD conjugated SWNTs) and control groups (nonconjugated SWNTs). Raman spectral analysis revealed consistent accumulation of SWNTs in the

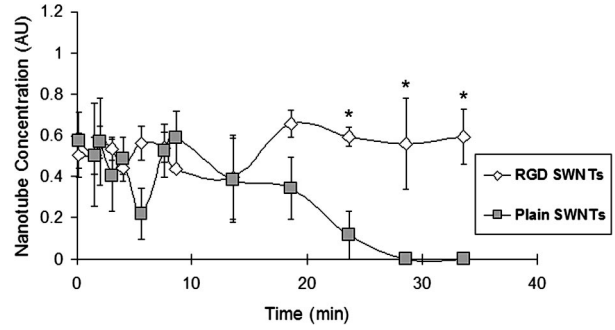

Figure 1. Pharmacokinetics of RGD SWNTs ($n = 3$) and plain nontargeted SWNTs ($n = 3$) in the tumor of nude mice over time. Notice the accumulation of RGD nanotubes (gray diamonds) in the tumor slightly increases over time remaining within the tumor area. Plain nanotubes (open-faced squares) appear to initially arrive in the tumor with a rapid decrease after 20 min postinjection. Data are presented as mean ± standard error, and * indicates $p < 0.05$.

tumors of the experimental mice as opposed to the tumors of the control mice which showed initial accumulation of SWNTs with a rapid decrease after 20 min post injection (Figure 1). The data points revealed a statistical difference in accumulation of SWNTs between the tumors of the experimental and control groups after 20 min with a $p < 0.05$.

Following dynamic Raman imaging, Raman mapped images of the tumor area were acquired in both groups with a raster scan at 2, 8, 24, 48, and 72 h postinjection with a step size of 750 μm and an integration time of 3 s. The images acquired from the experimental mice receiving conjugated RGD nanotubes showed increased Raman signal at all time points in the tumor area suggesting effective targeting of the RGD nanotubes to the integrin expressing tumor (U87MG cell line). Notice how the tumor is easily defined and the intensity remained constant throughout all time points out to 72 h in the experimental group (Figure 2). Conversely, the Raman images acquired from the tumor area of the control group showed either minimal or no Raman signal from the nontargeted nanotubes with no clearly identifiable tumor margins.

Raman spectra of the entire tumor region from each of the maps acquired above were processed at 2, 8, 24, 48, and 72 h postinjection of SWNTs for quantitative analysis. Mice in the experimental group which received RGD conjugated SWNTs showed a trend where nanotubes increased in accumulation in the tumor over 24 h and then continued to stay in the tumor out to 72 h postinjection. The control group that received nontargeted nanotubes showed little to no accumulation of SWNTs in the tumor from 2 to 72 h postinjection. Statistical analysis showed a significant difference ($p < 0.05$) between the accumulation of SWNTs in the tumors of experimental and control groups at all time points (Figure 3). This correlated with the kinetics data where decreased accumulation of nanotubes in the control group was observed in the tumor after 20 min postinjection.

Raman spectra of the contralateral shoulder in each group were also acquired at 2, 8, 24, 48, and 72 h postinjection to determine nonspecific localization of SWNTs in the shoulder

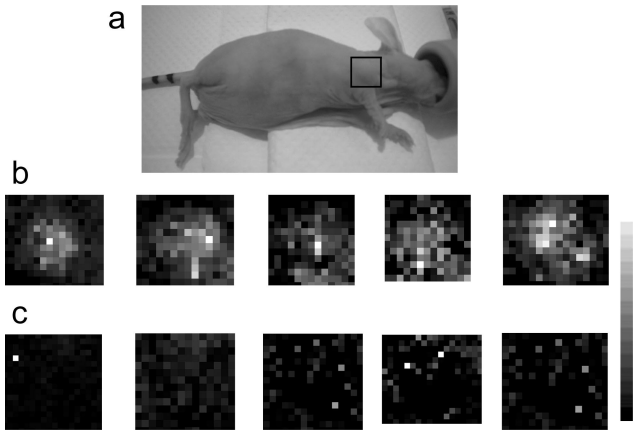

Figure 2. Raster-scan images of tumor area (750 μm steps) using Raman spectroscopy in conjunction with SWNTs. The grayscale bar to the right depicts the Raman intensity where white represents the maximum intensity and black represents no intensity. (a), Digital photograph of tumor bearing mouse depicting tumor area scanned with Raman spectroscopy (black box). (b), Panel of tumor maps from mouse receiving RGD nanotubes at various time points post injection starting from left to right with 2, 8, 24, 48, and 72 h. (c), Panel of tumor maps from mouse receiving plain nanotubes at various time points post injection starting from left to right with 2, 8, 24, 48, and 72 h. Notice how the panel of tumor maps in panel b from the mouse that received RGD nanotubes shows a continued accumulation of nanotubes in the tumor area over 72 h, as opposed to panel c which shows no defined accumulation of nanotubes in the tumor area of a mouse that received plain nanotubes.

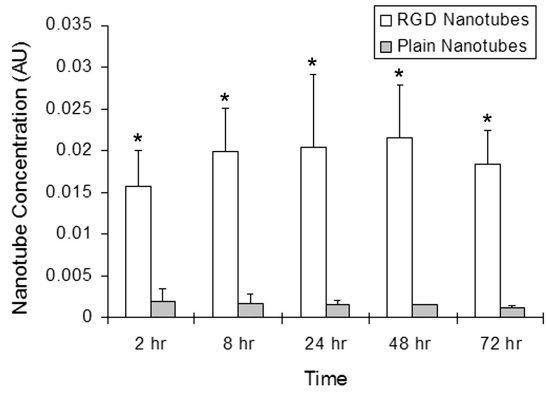

Figure 3. Raman spectral analysis of RGD nanotubes and plain nontargeted nanotubes within the tumor over three days post injection (error bars represent s.e.m.). The graphed data show a significant difference (* indicates $p < 0.05$) between mice injected with RGD nanotubes and mice injected with plain nanotubes at all time points post injection.

area. Individual Raman spectra were acquired in all mice over a single point focusing on either the contralateral shoulder or the tumor site for 10 s. This data revealed little to no accumulation of the RGD conjugated SWNTs or the nontargeted plain SWNTs in the contralateral shoulder. Comparisons between the tumor and contralateral shoulder in the experimental group showed a significant difference ($p < 0.05$) at all the time points (Figure 4). However no difference was seen between the tumor and contralateral shoulder in the control group as was expected (data not shown). These results suggest that nonspecific targeting of the SWNTs is minimal and should not influence the increased

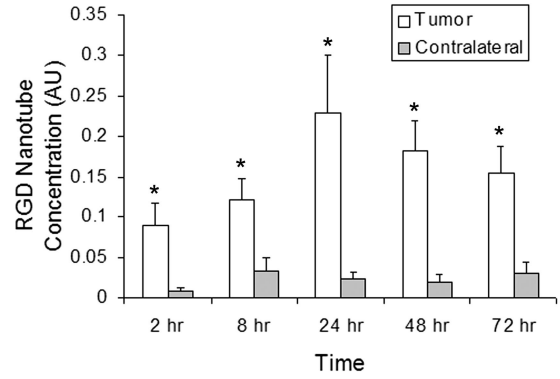

Figure 4. Raman spectral analysis comparing accumulation of RGD nanotubes within the tumor area on the right shoulder and the contralateral left shoulder (no tumor) of nude mice (error bars represent s.e.m.). Notice the significant increase (* indicates $p < 0.05$) of RGD nanotube accumulation within the tumor area as opposed to the contralateral shoulder at all time points over three days.

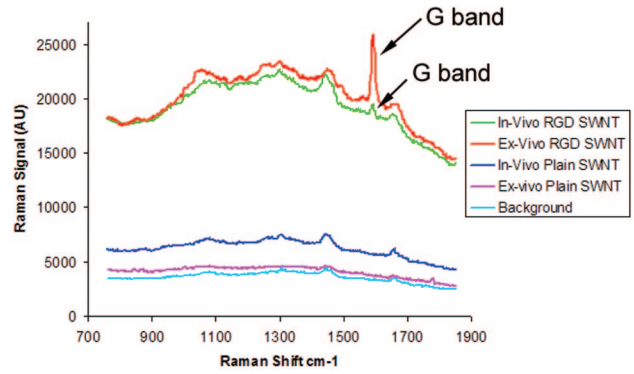

Figure 5. Raman spectrum acquired from in vivo (red) and ex-vivo (green) tumors at 72 h in both experimental and control groups of mice. Notice how the g-band Raman peak (arrow $\sim$ 1593 cm^{-1}) is prominently pronounced in the experimental group where mice received RGD conjugated nanotubes. Conversely, there is no g-band Raman peak associated with the nanotubes seen in either the in vivo (blue) or ex-vivo (purple) tumors taken from the mice that received nontargeted plain nanotubes. The spectrums given from the control mice resemble the background spectrum (light blue) taken of the tumors before nanotube injection.

accumulation of RGD conjugated nanotubes seen in the tumor.

After the 72 h time point, mice were sacrificed and the liver, spleen and tumor were collected for Raman imaging and histopathological examination. The ex-vivo Raman spectra of the tumor correlated well with the in vivo Raman data collected at 72 h as seen in Figure 5. Raman mapping of the excised tumor (SI Figure 2a) also revealed well defined localization of the RGD conjugated SWNTs in the tumor as opposed to the mice receiving nontargeted nanotubes which showed little to no localization in the tumor (SI Figure 2b). Raman spectra analysis and mapping revealed nanotube accumulation in the excised liver and spleen of both experimental and control animals (SI Figure 3). This is attributed to the short circulation time of these nanoparticles and natural uptake of SWNTs by the reticuloendothelial system. However a trend was observed where the ex-vivo Raman data shown in Figure 6a suggested that the control

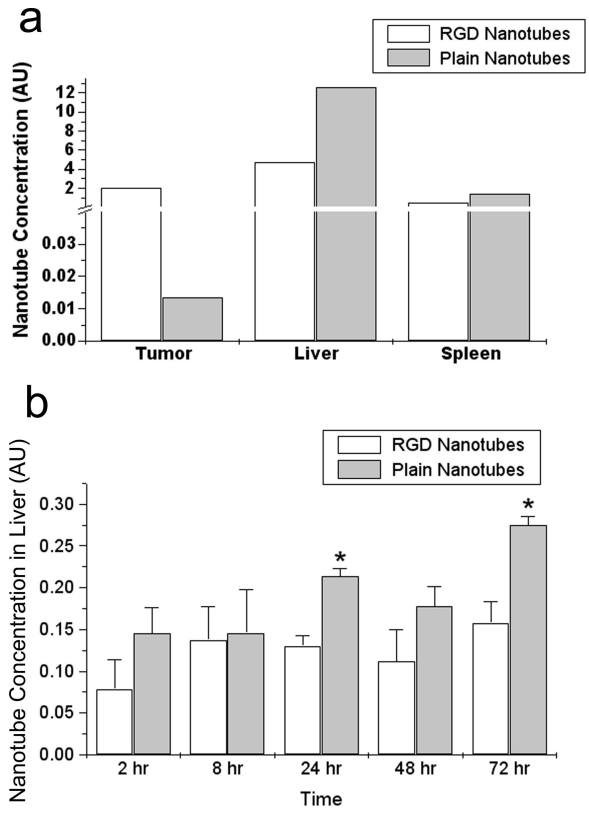

Figure 6. Raman spectral analysis of RGD and plain nanotube accumulation within various tissues from experimental and control mice (error bars represent s.e.m.). (a), Raman data of various excised tissues at 72 h post nanotube injection. Excised tumor data shows more accumulation of RGD nanotubes within tumor tissue than plain nanotubes at 72 h, supporting in vivo data shown previously. The graph also depicts more accumulation of plain nanotubes within the excised liver and spleen in comparison to the mice that received RGD conjugated nanotubes. (b), In-vivo Raman data of RGD nanotubes and plain nontargeted nanotubes within the liver over three days post injection. Notice how the 72 h time point shows roughly twice as much nanotube accumulation in the liver of mice receiving plain nanotubes, correlating with the 72 h ex-vivo data in panel a. Significant differences in nanotube accumulation within the liver were observed at 24 and 72 h post injection with a $p < 0.05$ depicted with *. Very little Raman signal was seen throughout the control group; therefore a *y*-axis break was placed between 1 and 0.04 to visualize lower nanotube concentration in tumors of mice receiving plain nanotubes.

group had more nanotube accumulation in the liver than the experimental group. This also correlated with the in vivo Raman data taken from the liver in both groups as shown in Figure 6b. Mice receiving nontargeted nanotubes showed more accumulation of nanotubes in the liver than the mice receiving RGD nanotubes at 24 and 72 h with a $p < 0.05$. These results support the idea that because more RGD conjugated nanotubes accumulated in the tumor; less would be found in the liver when compared to the nontargeted nanotubes which localized almost completely in the liver and spleen of the control mice.

In this proof of principle study we have demonstrated that Raman spectroscopy has the potential to noninvasively localize targeting of SWNTs conjugated with RGD in an integrin expressing tumor model. The Raman G-band peak ($\sim$1593 cm^{-1}) associated with the graphite in SWNTs was easily identified over time from the noninvasive Raman spectra acquired in the tumors of the experimental mice receiving RGD nanotubes. Raman imaging of the excised tumor supported this noninvasive Raman data revealing the presence of RGD nanotube clusters in the tumor at 72 h postinjection. The lack of nanotube accumulation in the tumors of the control mice receiving nontargeted nanotubes was determined by the less intense to complete absence of the 1593 cm^{-1} Raman peak both in living mice and ex-vivo.

A more quantitative look shows the accumulation of RGD SWNTs in the tumor area was approximately 12 times higher than plain nontargeted SWNTs using our Raman microscope at 24 h post injection. A similar correlation was seen in a previously published biodistribution study using microPET.[7] However, the accumulation of ^{64}Cu-RGD SWNTs in the tumor area was only 4.6 times higher than plain nontargeted ^{64}Cu-plain SWNTs. This difference could be attributed to several factors including the limited depth of penetration with Raman imaging, and/or the difference in particle conjugation. Recall that the maximum depth of penetration observed with our Raman microscope in conjunction with SWNTs was approximately 2 mm, whereas the total tissue depth in our tumor model was on the order of 3 mm. Therefore, the total SWNT concentration in the tumor was not entirely evaluated which could explain the quantitative differences in RGD versus Plain SWNT uptake in our study as opposed to that of which was previously reported in Liu et al. using microPET where depth was not a limiting factor. In addition, SWNTs used in Liu et al.[7] had a 1:5 molar ratio of RGD to DOTA (metal chelator for radiolabeling) for conjugation via PEG_{5400} linker as opposed to our SWNTs which just used RGD conjugated via PEG_{5000} linker. The additional conjugation of DOTA would occupy more PEG linker sites leaving less for the tumor targeting RGD peptide. Therefore, our SWNTs would presumably have more RGD peptide conjugated to the SWNT surface thus improving the targeting ability of our RGD-SWNTs to tumor. Finally, the method described by Liu et al.[7] for SWNT detection and biodistribution uses a more indirect method by conjugating SWNTs to a ^{64}Cu radionuclide via a DOTA chelator, which has the potential to fall off, as opposed to our direct method of detecting the inherent Raman signal from the actual graphite of the SWNTs.

To date, several noninvasive preclinical imaging applications have been used to visualize integrin expression including MRI,[17] contrast-enhanced ultrasound,[18,19] NIR fluorescence,[20] bioluminescence,[21] SPECT, and PET.[15,16,22] Now that Raman spectroscopy has successfully shown the ability to noninvasively localize targeted RGD nanotubes in an integrin expressing tumor model, it too can be further developed as an ultrasensitive noninvasive detection modality for preclinical imaging applications. We are currently developing new Raman spectroscopy instrumentation for faster scanning times, better depth estimation, and potential tomographic imaging for absolute quantification of Raman signal. The development of new targeted Raman nanoparticles such as surface enhanced Raman scattering (SERS)[23−25] nanoparticles and composite organic inorganic nanoparticles (COINS)[26,27]

should also further expand the eventual utility of this unique imaging platform for noninvasive preclinical evaluation.

Thus far, the role of Raman spectroscopy in biomedical applications has been mostly limited to ex-vivo evaluation of cells and excised tissues.[2−6] Noninvasive Raman spectroscopy could provide longitudinal information in living subjects at various time points without having to sacrifice several animals. This relatively inexpensive and easy to use imaging system could also be used in conjunction with other imaging modalities such as microPET or MRI to achieve better depth and spatial information. Multimodal biomedical imaging can provide another degree of evidence to support the efficacy of novel therapeutic techniques. Investigators have recently developed SWNT/iron oxide nanoparticle complexes as multimodal biomedical imaging agents, combining the high contrast imaging power of MRI and the sensitivity of Raman.[28] A therapeutic potential also exists through phototherapy and hyperthermia effects with NIR laser excitation, and high frequency external magnetic field modulation.

Although other Raman nanoparticles exist, as mentioned above, carbon nanotubes have the added advantage of having an inherent Raman signature. No further labeling or encapsulation is needed to produce a Raman peak as in COINS and SERS nanoparticles.[23,26,27] Raman spectroscopy has proven to be a valuable tool for characterizing SWNTs. For instance, Raman spectroscopy has been used to differentiate between metallic and semiconducting nanotubes, and may also be employed to determine SWNT diameters and even nanotube chirality.[29,30] One paper discusses the use of Raman spectroscopy to differentiate between double wall nanotubes (DWNTs) and triple wall nanotubes (TWNTs).[31] Several new Raman peaks are seen in the radial breathing mode (RBM) region of the Raman spectrum for TWNTs. The authors claim that the new peaks are evidence that nanotubes with smaller diameters have been formed. The difference in Raman spectra between DWNTs and TWNTs resulting from their different diameters may give rise to multiplexing capabilities with nanotubes, where two nanoparticles can be simultaneously injected with different tags and easily distinguished with Raman imaging.

One problem that exists when using nanotubes in conjunction with Raman spectroscopy is their lower sensitivity when compared with COINS and SERS nanoparticles. It was determined by our laboratory that nanotubes are roughly 1400 times less Raman intense than SERS nanoparticles based on a per particle analysis. However it has been recently reported that carbon nanotubes adsorbed onto metal surfaces increase their Raman signal.[32] The introduction of silver nanoparticles into the carbon nanotubes film results in the SERS effect increasing the intensity of the Raman spectrum. This plasmonic phenomenon is referred to as surface enhanced Raman scattering where molecules adsorbed onto nanoroughened noble metal surfaces experience a dramatic increase in the incident electromagnetic field producing high Raman intensity. SERS enhances detection sensitivity up to 10−14 orders of magnitude over conventional Raman spectroscopy and is employed in both COINs and SERS nanoparticles.[23,26,27]

Other carbon-based Raman active nanomaterials such as single wall nanohorns (SWNHs) have also shown great potential for applications in drug delivery systems.[33] SWNHs are a new type of carbon-based nanoparticle derived from SWNTs. They typically consist of a 2−5 nm tube diameter and 30−50 nm length with a closed cone head at one extremity. SWNHs aggregate and give rise to spherical structure with a diameter of about 100 nm, a size that would benefit from enhanced permeability in solid tumors. The biggest advantage of this nanoparticle is its porosity and large surface area which allows for great affinity with organic compounds. These new nanomaterials have been functionalized for targeting and are currently being further developed for drug delivery. Their inherent Raman Effect would make them ideal candidates for imaging with our noninvasive Raman imaging system to assess drug delivery and therapeutic efficacy in small animal models.

In conclusion, Raman spectroscopy's ability to noninvasively localize targeted SWNTs in a tumor model sets the foundation for future studies with other targeted Raman nanoparticles. The current work supports further development of this highly sensitive noninvasive Raman imaging tool to asses the efficacy of new diagnostic strategies and therapies in small animal models, thus leading to improvements in the eventual care of cancer patients.

Acknowledgment. We thank Drs. Bill Doering, Glenn Davis, Ian Walton, and David Guagliardo at Oxonica for their assistance with SENSERSee Software. We would also like to thank Dr. Zhenhuan Chi (Rensihaw) and Dr. Timothy Doyle (Stanford Small Animal Imaging) for their support. This work was funded in part by NCI CCNE U54 CA119367 (SSG), NIBIB BRP 5-RO1-EBB000312 (SSG), and ICMIC P50 CA114747 (SSG). C.Z. received support from NIH Training grant T32 CA09695-15 Advanced Techniques for Cancer Imaging.

Supporting Information Available: Procedures for cell targeting study, phantom preparation, SWNT conjugation with RGD, animal model preparation, and details on Raman image acquisition and analysis. This material is available free of charge via the Internet at http://pubs.acs.org.

References

(1) Ryder, A. G. *Curr. Opin. Chem. Bio.* **2005**, *9*, 489.
(2) Hanlon, E. B.; Manoharan, R.; Koo, T. W.; Shafer, K. E.; Motz, J. T.; Fitzmaurice, M.; Kramer, J. R.; Itzkan, I.; Dasari, R. R.; Feld, M. S. *Phys. Med. Biol.* **2000**, *45*, R1.
(3) Haka, A. S.; Shafer-Peltier, K. E.; Fitzmaurice, M.; Crowe, J.; Dasari, R. R.; Feld, M. S. *PNAS* **2005**, *102*, 12371.
(4) Stuart, D. A.; Yuen, J. M.; Shah, N.; Lyandres, O.; Yonzon, C. R.; Glucksberg, M. R.; Walsh, J. T.; Van Duyne, R. P. *Anal. Chem.* **2006**, *78*, 7211.
(5) Lee, S.; Kim, S.; Choo, J.; Shin, S. Y.; Lee, Y. H.; Choi, H. Y.; Ha, S.; Kang, K.; Oh, C. H. *Anal. Chem.* **2007**, *79*, 916.
(6) Kneipp, J.; Kneipp, H.; McLaughlin, M.; Brown, D.; Kneipp, K. *Nano Lett.* **2006**, *6*, 2225.
(7) Liu, Z.; Cai, W.; He, L.; Nakayama, N.; Chen, K.; Sun, X.; Chen, X.; Dai, H. *Nature Nanotechnol.* **2007**, *2*, 47.
(8) Keren, S.; Zavaleta, C.; Cheng, Z.; de la Zerda, A.; Gheysens, O.; Gambhir, S. S. *Proc. Natl. Acad. Sci. U. S. A.* **2008**, n/a.

(9) Cherukuri, P.; Gannon, C. J.; Leeuw, T. K.; Schmidt, H. K.; Smalley, R. E.; Curley, S. A.; Weisman, R. B. *Proc. Natl. Acad. Sci. U. S. A.* **2006**, *103*, 18882.
(10) Cuenca, A. G.; Jiang, H.; Hochwald, S. N.; Delano, M.; Cance, W. G.; Grobmyer, S. R. *Cancer* **2006**, *107*, 459.
(11) Lacerda, L.; Bianco, A.; Prato, M.; Kostarelos, K. *Adv. Drug Delivery Rev.* **2006**, *58*, 1460.
(12) Meyer, A.; Auernheimer, J.; Modlinger, A.; Kessler, H. *Curr. Pharm. Des.* **2006**, *12*, 2723.
(13) Dunehoo, A. L.; Anderson, M.; Majumdar, S.; Kobayashi, N.; Berkland, C.; Siahaan, T. J. *J. Pharm. Sci.* **2006**, *95*, 1856.
(14) Chen, X. *Mini. Rev. Med. Chem.* **2006**, *6*, 227.
(15) Wu, Y.; Zhang, X.; Xiong, Z.; Cheng, Z.; Fisher, D. R.; Liu, S.; Gambhir, S. S.; Chen, X. *J. Nucl. Med.* **2005**, *46*, 1707.
(16) Zhang, X.; Xiong, Z.; Wu, Y.; Cai, W.; Tseng, J. R.; Gambhir, S. S.; Chen, X. *J. Nucl. Med.* **2006**, *47*, 113.
(17) Sipkins, D. A.; Cheresh, D. A.; Kazemi, M. R.; Nevin, L. M.; Bednarski, M. D.; Li, K. C. *Nat. Med.* **1998**, *4*, 623.
(18) Dayton, P. A.; Pearson, D.; Clark, J.; Simon, S.; Schumann, P. A.; Zutshi, R.; Matsunaga, T. O.; Ferrara, K. W. *Mol. Imaging* **2004**, *3*, 125.
(19) Leong-Poi, H.; Christiansen, J.; Klibanov, A. L.; Kaul, S.; Lindner, J. R. *Circulation* **2003**, *107*, 455.
(20) Wang, W.; Ke, S.; Wu, Q.; Charnsangavej, C.; Gurfinkel, M.; Gelovani, J. G.; Abbruzzese, J. L.; Sevick-Muraca, E. M.; Li, C. *Mol. Imaging* **2004**, *3*, 343.
(21) Niu, G.; Xiong, Z.; Cheng, Z.; Cai, W.; Gambhir, S. S.; Xing, L.; Chen, X.*Mol. Imaging Biol.* **2007**, n/a.
(22) Haubner, R.; Weber, W. A.; Beer, A. J.; Vabuliene, E.; Reim, D.; Sarbia, M.; Becker, K. F.; Goebel, M.; Hein, R.; Wester, H. J.; Kessler, H.; Schwaiger, M. *PLoS Med.* **2005**, *2*, e70.
(23) Mulvaney, S. P.; Musick, M. D.; Keating, C. D.; Natan, M. J. *Langmuir* **2003**, *19*, 4784.
(24) Qian, X.; Peng, X. H.; Ansari, D. O.; Yin-Goen, Q.; Chen, G. Z.; Shin, D. M.; Yang, L.; Young, A. N.; Wang, M. D.; Nie, S. *Nat. Biotechnol.* **2008**, *26*, 83.
(25) Souza, G. R.; Levin, C. S.; Hajitou, A.; Pasqualini, R.; Arap, W.; Miller, J. H. *Anal. Chem.* **2006**, *78*, 6232.
(26) Su, X.; Zhang, J.; Sun, L.; Koo, T. W.; Chan, S.; Sundararajan, N.; Yamakawa, M.; Berlin, A. A. *Nano Lett.* **2005**, *5*, 49.
(27) Sun, L.; Sung, K. B.; Dentinger, C.; Lutz, B.; Nguyen, L.; Zhang, J.; Qin, H.; Yamakawa, M.; Cao, M.; Lu, Y.; Chmura, A. J.; Zhu, J.; Su, X.; Berlin, A. A.; Chan, S.; Knudsen, B. *Nano Lett* **2007**, *7*, 351.
(28) Choi, J. H.; Nguyen, F. T.; Barone, P. W.; Heller, D. A.; Moll, A. E.; Patel, D.; Boppart, S. A.; Strano, M. S. *Nano Lett.* **2007**, *7*, 861.
(29) Dillon, A. C.; Yudasaka, M.; Dresselhaus, M. S. *J. Nanosci. Nanotechnol.* **2004**, *4*, 691.
(30) Dresselhaus, M. S.; Dresselhaus, G.; Jorio, A.; Souza Filho, A. G.; Samsonidze, G. G.; Saito, R. *J. Nanosci. Nanotechnol.* **2003**, *3*, 19.
(31) Qiu, H.; Shi, Z.; Gu, Z.; Qiu, J. *Chem. Commun. (Camb)* **2007**, 1092.
(32) Hu, X.; Wang, T.; Wang, L.; Guo, S.; Dong, S. *Langmuir* **2007**, n/a.
(33) Shiba, K. *J. Drug Targeting* **2006**, *14*, 512.

NL801362A